Volume 1 | Number 1 | Jan 2013 | Pages 1–100

Nanoscale

www.rsc.org/nanoscale

ROYAL SOCIETY OF CHEMISTRY

ROYAL SOCIETY OF CHEMISTRY

www.rsc.org/nanoscale

High-yield fabrication of nm-size gaps in monolayer CVD graphene[†]

Cornelia Nef,[*a] **László Pósa,**[b] **Péter Makk,**[a,b] **Wangyang Fu,**[a] **András Halbritter,**[b] **Christian Schönenberger,**[a] **and Michel Calame**[*a]

Herein we demonstrate the controlled and reproducible fabrication of sub-5 nm wide gaps in single-layer graphene electrodes. The process is implemented for graphene grown via chemical vapor deposition using an electroburning process at room temperature and in vacuum. A yield of over 95% for the gap formation is obtained. This approach allows producing single-layer graphene electrodes for molecular electronics at a large scale. Additionally, from Raman spectroscopy and electroburning carried out simultanously, we can follow the heating process and infer the temperature at which the gap formation happens.

The perfect electrode material for molecular electronics should be mechanically stable, planar and offer flexible molecular anchoring possibilities[1,2]. Planarity will in particular grant an easier access for top-gating experiments as well as facilitate optical and mechanical (scanning probe) imaging. Until now, gold is the preferred electrode material as it allows a covalent or coordinative binding of the molecules for several binding groups, is inert to most chemical environments and remains relatively easy to handle. Gold however also presents major disadvantages: the relatively thick metal electrodes lead to a large screening of a backgate potential; the existence of too many binding geometries leads to ill-defined metal-molecule-metal junction conductances; and the important mobility of surface atoms at room temperature strongly limits the junctions mechanical stability[3,4]. Other metals like Pt and Ag have been used to measure junctions formed by molecules[5–8]. The reactivity of these metals with oxygen however limits these experiments. A particularly promising approach is based on carbon nanotubes (CNTs)[9–11] and graphene[12–16]. Organic molecules can strongly couple to such

electrode systems by $\pi - \pi$ stacking[12,17,18] or through covalent bonds[9,15] and their thickness is similar to the size of the molecules investigated. Graphene is especially interesting as it can be produced in large scale through chemical vapor deposition (CVD)[19–21] or growth on silicon carbide[22], a prerequisite to gather the large statistics required in molecular electronics investigations. Graphene as an electrode material for contacting molecules has been the subject of various theoretical studies[23–25]. First experiments using CNTs[9–11], few-layer graphite[12–14] and CVD graphene[15,16] show that sp[2] carbon electrodes are stable and allow gating, optical and chemical access. **So far, electrodes fabricated through electroburning (EB) showed a limited yield, reaching at the very best 50%[10,26]. A fine patterning of graphene is possible using advanced beam-based nanofabrication and in particular via helium-ion-beam-lithography (HIBL), see e.g.[27,28]. The fabrication of nanoscale gaps via direct cutting of CNTs using HIBL was for instance recently demonstrated[11]. Carbon electrodes have also been fabricated using electron-beam based methods[9,15]. Beam-based techniques remain however delicate to control for gaps below 5 nm and an imporvement of the yield comes at the cost of increased complexity and lower speed[29].**

In this letter, we report a **simple and rapid** method for fabricating nanometer-sized gaps in single-layer CVD graphene at a high yield. We use the EB of graphene, a process were the current in a system is increased until electrical breakdown[12]. Current induced sublimation of carbon atoms in high vacuum has been shown to narrow multilayer graphene to nanometer sized constrictions[30,31]. The formation of quantum dots and single atom chains has been claimed[32–35] as well as the fabrication of small gaps in CNTs[10] and few-layer graphene[12,26]. At ambient pressure, the breakdown is likely to be a consequence of the oxidation of carbon atoms, triggered by the local self-heating caused by the large current densities[10,12,36]. To control the burning process and avoid a blow-up of the junction, we performed our measurements at a reduced oxygen pressure, **under a vacuum of $\approx 10^{-5}$ mbar**. Raman spectroscopy has been used to investigate heat generation in graphene constrictions[37,38], so performing Raman spectroscopy and EB simultaneously gives us an insight in the
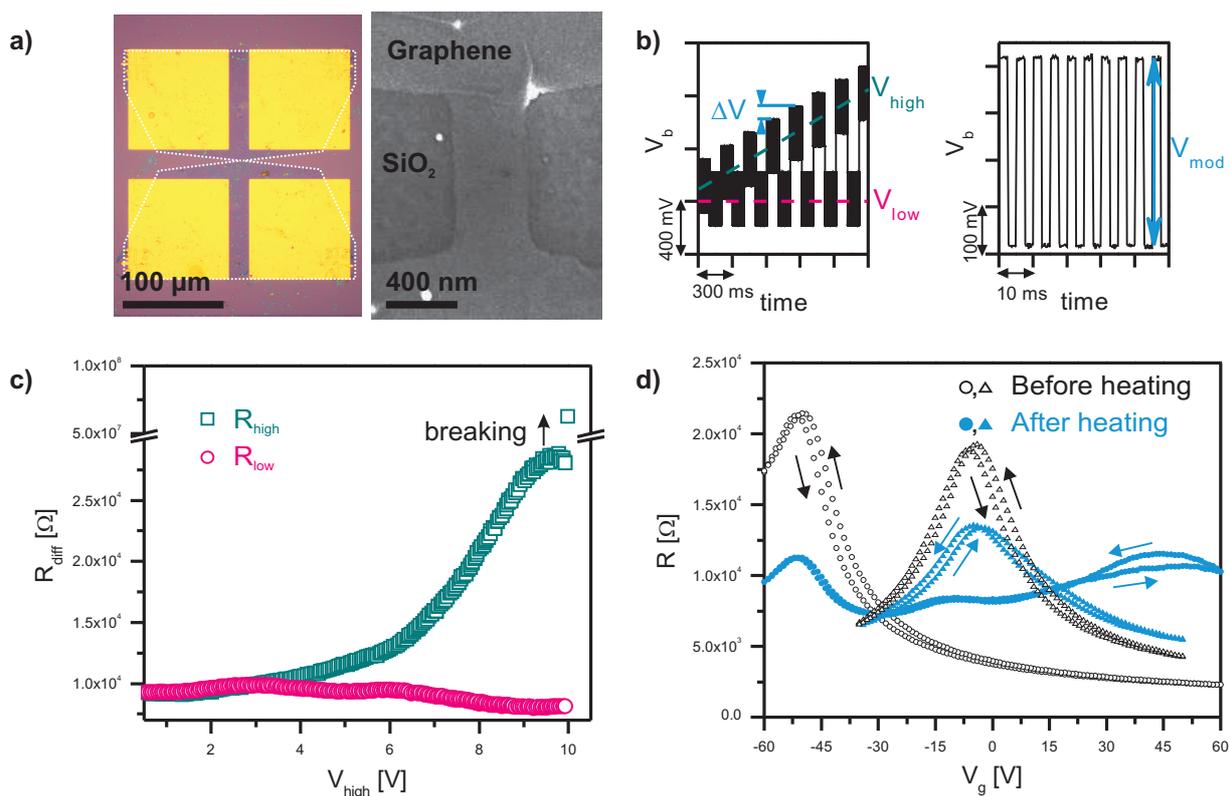
Fig. 1 a) Optical (left) and scanning electron microscopy (right) images of a typical sample. The white dashed line in the optical image shows the borders of the graphene flake. b) Bias voltage V_b during the EB process. We alternate a high V_{high} and low V_{low} bias voltage superposed with a modulation V_{mod} to measure the differential resistance. V_{high} is increased in steps of ΔV. c) Differential resistance at high R_{high} (dark cyan squares) and low R_{low} (pink circles) bias during EB of a device. d) Gate dependent resistance before (black open symbols) and after (blue solid symbols) heating the sample while performing the EB process but stopping it before breakdown. Two different samples are shown (circles and triangles).

temperatures reached.

For our samples we use single-layer graphene obtained from CVD growth on copper[19–21] and transfered onto doped silicon substrates coated with 300 nm of thermal oxide[20,39,40]. Patterning is done either using electron-beam-lithography or UV-lithography, followed by argon - oxygen plasma etching. The graphene is shaped into 400 nm to 600 nm or 2 μm wide constrictions. Contacts are patterned by an additional lithography step followed by the evaporation of 40 nm of gold with a 5 nm titanium adhesion layer. In contrast to the required custom design for samples made from exfoliated graphene, the same predefined masks can be used to produce 100 - 400 devices on one chip with our CVD graphene process. An optical image of a device and a scanning electron microscopy (SEM) picture of a constriction are shown in figure 1a). The wider devices are used for Raman spectroscopy performed at the same time as the EB procedure. The initial resistance of the devices at low bias and floating back gate is typically between 2 kΩ and 20 kΩ.

To burn the graphene constrictions a process was adapted from previous studies on gold electromigration[41]. The bias voltage is alternated between a high and a low value (V_{high} and V_{low}) to which a modulation (V_{mod}) is superimposed to measure the differential resistance ($\frac{\Delta I}{V_{mod}}$, where I is the measured current) at high R_{high} and low R_{low} bias. Both, V_{low} and V_{mod} are set to 0.4 V. V_{high} is ramped stepwise with $\Delta V = 0.1$ V, as shown in figure 1b). The alternating bias voltage V_b allows us to distinguish between effects which change the resistance of the graphene constriction and affect both R_{high} and R_{low} from Joule heating which only influences R_{high}.

We first consider the heating process in the junction. Figure 1c) shows the evolution of R_{high} and R_{low} for a typical burning process of a highly doped sample. R_{high} increases, whereas R_{low} stays almost constant. This is an effect of Joule heating, which leads to nonlinear current-voltage characteristics[42,43]. We observe this until the graphene bridge breaks and R_{high} jumps to a high value (arrow), faster than the time resolution of our setup (which is 10 ms). With the setup used for break-

ing, this resistance value can not be resolved anymore and just represents the noise level. At this point V_b is set back to 0 V. The graphene constrictions are burned in a single step without the use of a feedback.

Figure 1d) (black) shows the gate behavior of graphene constrictions right after fabrication, where the different symbols represent two different devices. The charge neutrality point (CNP) can be clearly seen at a gate voltage $V_g \approx -50$ V for the first device, and is close to 0 V for the second. This is due to slight differences in the fabrication process, leading to distinct surface doping. If the EB procedure is applied, but stopped before the electrical breakdown, the behavior of R vs V_g changes dramatically for the heavily doped sample. Additional peaks appear at ≈ -15 V and ≈ 45 V. We attribute this effect to the redistribution of surface contaminants which can have a huge effect on the resistance behavior. It is well known, that applying high current densities can move particles on top of the graphene[46,47] resulting in a cleaning of the surface. In particular cases, this mechanism has been implemented to prepare clean graphene structures showing ballistic transport[48–50]. In our samples, most of the heat dissipation takes place over the device constriction and contaminants move away to the colder contact areas. Applying a second heating step did not lead to further significant changes. To ensure that the resistance is only influenced by heating and not by doping contaminants, we focus on results for annealed devices, where the EB was performed directly after the heating. If the burning procedure is performed close to the CNP, this can lead to a resistance behavior quite different from the one shown in figure 1c). We observe that the gate behavior after heating changes within minutes to hours in vacuum at room temperature, showing that the contaminants can slowly diffuse back to the constriction.

Raman spectroscopy can act as a local thermometer for graphene[51] as the 2D peak position shifts linearly with temperature and is independent of the carrier density. We performed Raman spectroscopy and EB simultaneously to estimate the heat generated at the graphene constriction. We used a WITec alpha300r confocal Raman microscope together with an Olympus MPlanFL 100x objective for characterization and an Olympus LMPlanIR 50x long working distance objective for the combined electrical and optical measurements. A laser of 532 nm wavelength was used and the laser power was set to 2 mW. These measurements were performed in ambient conditions on devices with a constriction of 2 μm.

To calibrate our system, we did Raman measurements on our graphene samples during external heating. All peaks were fitted with a Lorentzian function. A linear shift was observed for the graphene 2D peak located at ≈ 2688 1/cm (figure 2a)) and for the graphene D peak at ≈ 1350 1/cm (right inset figure 2a). For the graphene G peak at ≈ 1586 1/cm no significant shift was observed. Our system showed a shift of -0.051 1/cmK and -0.016 1/cmK for the 2D and D peak respectively.

The shift of the D peak is smaller, as only one phonon is involved whereas the 2D peak involves the scattering of two phonons. The shift of the Si peak at ≈ 520 1/cm (left inset figure 2a) was fitted with a model for inelastic scattering[44,45]. The extracted values can be found in the supporting information.

After calibrating the temperature dependence of the Raman peaks, we can determine the temperature during the EB procedure. The spectra in the region of the 2D peak recorded during EB are plotted in figure 2b), the color code shows the increasing heating power P_{el}. A clear shift of the graphene 2D peak to lower wavenumber is observed, highlighted with a dashed line. We note that the peak intensity decreases with increasing P_{el} due to focus drift during the measurement. We take this effect into account by correcting the peak positions following the procedure described in the supporting information. The corrected shift of the graphene 2D peak with P_{el} is shown in figure 2c) (dots). Note that the power here is larger than in figure 1c) as we are now dealing with the wider graphene constrictions. Applying our calibration of -0.051 1/cmK to this data leads to temperatures up to 570 K before the electrical breakdown occurs, as plotted in figure 2c) (blue squares). Graphene oxidation has been found to start at ≈ 470 K and etch pits form spontaneously at ≈ 720 K[52], which agrees well with our findings. The power needed to break the graphene is substantially higher in vacuum where values of 1000 K for supported and 2000 K for suspended graphene were reported[37,53]. We note that this approach provides a temperature averaged over the laser spot size (≤ 400 nm diameter here). It is thus well possible that the effective temperature locally exceeds the values reported.

We now turn to the temperature behavior of the resistance in our devices. The heat generated in the constriction can be dissipated over different pathways, including the environment, the electrodes and the substrate. The heat flow to the environment can be assumed to be small, especially for the experiments performed in vacuum[37]. In graphene, most of the heat is relaxed over electron-phonon interface scattering[54]. The phonon mean free path λ_{ph} of supported graphene at room temperature has been found to be $\lambda_{ph} \approx 100$ nm[55]. We thus assume to be in a diffusive regime for heat transport. Three kind of phonons can contribute to this: acoustic and optical phonons of the graphene as well as remote interface phonons (RIPs) forming at the SiO_2 graphene interface[56–58]. As the electrodes are separated by ≈ 20 μm we expect most of the heat to be dissipated over the substrate, not at the contacts[37,43,55]. This leads to a moderate heating of the whole chip, causing a shift of the Si Raman peak. The corresponding temperatures are plotted in figure 2c) as purple triangles, which shows that for this device the substrate heats up by 34 K. The broad samples need a much larger power than the thin ones to be broken. This is an effect of the larger
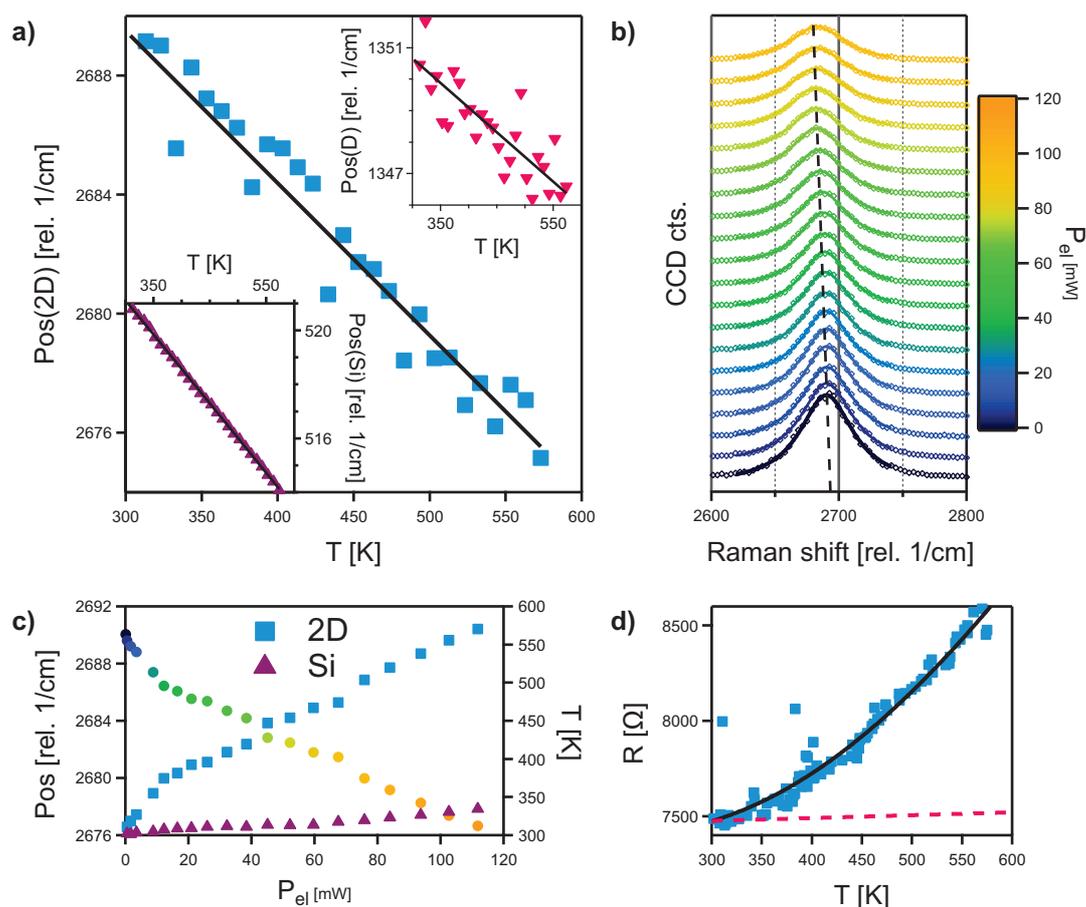
Fig. 2 a) Temperature dependence of the position of the graphene 2D Raman peak, the graphene D peak (right inset) and the Si peak (left inset) as well as linear fits for the graphene peaks and a fit based on the model of [44,45] for Si. b) Raman spectra around the graphene 2D peak recorded during the EB process. The color code shows the increasing electrical power P_{el}. The dashed line serves as a guide to the eye for the shift of the peak position. c) Corrected shift of the graphene 2D peak versus power P_{el} (dots), with the same color code is as for figure b), and corresponding graphene (blue squares) and silicon (purple triangles) temperature. d) Dependence of the graphene resistance on the temperature during EB, as well as a line with a slope of 0.15 Ω/K (pink dashed) and a fit according to equation 1 (black solid).

area, which leads to a larger cooling power over the substrate. The simplest model considering only scattering via low energy phonons (acoustic) would lead to a linear behavior of $R(T)$. However, if we consider $R(T)$ measured during EB (figure 2d), a linear fit leads to a proportionality factor $\alpha = 3.9$ Ω/K. This value is more than 1 order of magnitude larger than reported [56,59]. We therefore consider the following model for the temperature dependence of the graphene resistivity on a SiO$_2$ surface: [56,57]

$$\rho(T) = \rho_0 + \underbrace{\alpha T}_{\rho_A} + \underbrace{\beta \left(\frac{1}{e^{E_0/k_B T} - 1} \right)}_{\rho_B}, \qquad (1)$$

where ρ_0 is the residual resistivity at low temperature, E_0 is a phonon energy and α and β are constants. ρ_A is the resistivity due to acoustic phonon scattering and ρ_B is the resistivity due to scattering with optical phonons and / or RIPs. The pink dashed line in figure 2d) shows the evolution of ρ_A where we used the literature value of $\alpha = 0.15$ Ω/K [56,59]. This shows that this term is actually negligible here. Fitting our data to equation 1 leads to $\rho_0 = 7349$ Ω, $\beta = 18438$ Ω and $E_0 = 140.7$ meV (black curve). β depends on the carrier density n, which we assume to be approximately constant at high doping. The surface phonons of SiO$_2$ are predicted at ≈ 59 meV and ≈ 155 meV [56,57] and the graphene A_1' phonon, which has the largest electron-phonon coupling, is at ≈ 149 meV [42]. Our value for E_0 is similar to the above phonon energies. This confirms that electron scattering via optical phonons and / or RIPs is dominant in our graphene devices. Note that this analysis is only valid for measurements performed far from the CNP for a saturating charge carrier density.

We now look in more details at the formation of nanoscale

gaps at the graphene constrictions. After EB the graphene tunnel junctions were further analyzed using Raman spectroscopy and SEM and electrical measurements were performed. Figure 3a) shows the Raman spectra on the graphene electrodes (blue) and on the broken constriction (purple). The inset shows an intensity map for the graphene 2D peak. As the resolution of the Raman microscope is ≈ 400 nm, the constriction can only be hardly seen. The spectrum on the graphene electrode shows the signature of monolayer graphene, exhibiting a small defect induced peak (D peak). A larger D peak is observed in the spectrum on the constriction due to scattering at the edges or on defects introduced through the EB process. A slightly enhanced background between the D and the G peak and a substantial change in the G to 2D intensity ratio is observed on the constriction. This indicates the presence of disordered graphene or amorphous carbon, which could have been created during EB. The SEM image on the right shows the bridge after EB (lighter gray graphene, darker gray substrate), the gap is visible as a thin line emphasized by the arrows. **An additional topographic analysis of the gaps using AFM is given in the supporting information.**

Of the 50 samples burned in vacuum, 49 showed measurable tunnel current after EB, corresponding to a yield of 98%. In figure 3b) current-voltage characteristics for a typical sample are plotted. Before breaking (blue, right axis) the samples show linear behavior with a resistance of $13, 8$ kΩ. After EB (purple, left axis) the device shows S-shaped I-V curves, characteristic for tunneling. The linear fit to the low bias part (± 0.3 V) yields a 220 MΩ resistance. Assuming a rectangular barrier, we can fit the curves to the Simmons model[60] and obtain a gap size of ≈ 1.5 nm, for this device. The details of the fitting procedure are provided in the supporting information. Briefly, the three parameters fitted with the Simmons model are the junction area A, the barrier height Φ_b and the gap size d. The first two parameters are not robust, as good fits are possible with largely distinct values for these parameters. However, the gap distance d is more robust. **An overall range for d between 0.3 nm and 2.2 nm was obtained for our devices. A narrow distribution of the gap size is expected as the current depends exponentially on the distance between the electrodes. A change in the gap size would lead to a much larger change in the tunnel current and it would not be measurable anymore for large d.** From the ten samples burned in ambient conditions, only two showed a tunneling behavior. The control of the partial pressure of oxygen is thus crucial for generating small gaps in graphene, as also observed for the EB of CNTs[10]. The statistics for samples burned in vacuum and samples burned in ambient are shown in figure 3c). If a device did not show a tunneling current (we set the limit at 10 pA for ± 10 V bias), it is considered as fail. If the EB process was successful a linear curve was fitted to ± 0.3 V to extract the final resistance. These final resistances
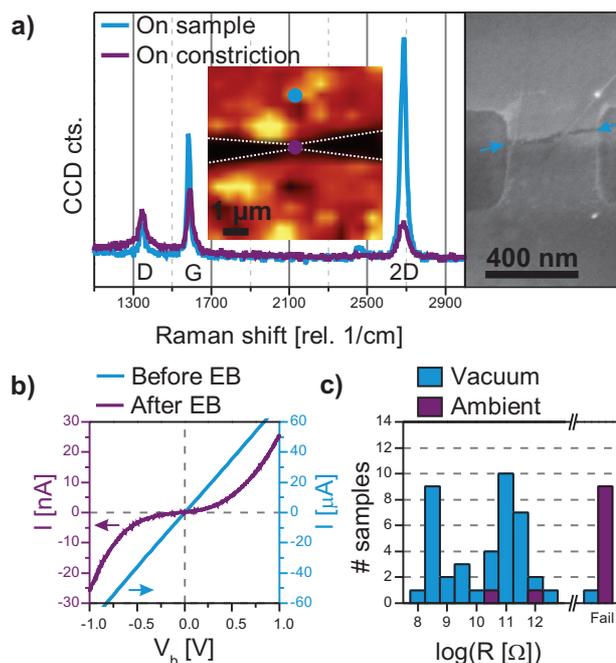

Fig. 3 a) Raman spectra recorded on the graphene electrode (blue) and on the burned constriction (purple). The inset shows a map of the integral over the graphene 2D peak, where the white dashed line shows the border of the graphene. A SEM image of the graphene constriction after EB (lighter gray graphene, darker gray substrate) is shown on the left, where the gap in the graphene is visible as a thin line, marked with arrows. b) I-V curves before (blue, right axis) and after (purple, left axis) the breaking process. After the breaking a clear tunneling behavior is observed. c) Statistical results of the EB process for vacuum and ambient. The samples are sorted into two parts whether they show tunneling current between ± 10 V or not (failed). The resistances given results from a linear fit to ± 0.3 V.

range from 100 MΩ to 100 GΩ, which corresponds to a gap size of $1 - 2$ nm, and are plotted in a logarithmic scale. Our results show the very good reproducibility of the experimental approach implemented, which provides final resistance values after burning similar to what was observed for devices starting with few-layer graphene[12]. Our approach presents the major advantages to provide a very high yield and is based on single-layer CVD graphene which makes a large-scale fabrication possible.

In conclusion, we established an effective procedure for the fabrication of nanometer-sized gaps in monolayer graphene with a very high yield. The use of CVD graphene allows the production of a large number of devices. These achievements are major requirements for the development of graphene-based molecular electronics. Using Raman spectroscopy, we inferred the local temperature at the graphene constriction up to the electrical breakdown. The temperature dependence of

the junction resistance is in agreement with a heat dissipation mechanism dominated by the coupling of the graphene to the substrate.

Acknowledgments

References

1 E. Lörtscher, *Nat. Nanotechnol.*, 2013, **8**, 381–384.

2 J. Y. Son and H. Song, *Curr. Appl. Phys.*, 2013, **13**, 1157–1171.

3 M. Ratner, *Nat. Nanotechnol.*, 2013, **8**, 378–381.

4 K. Moth-Poulsen and T. Bjørnholm, *Nat. Nanotechnol.*, 2009, **4**, 551–6.

5 O. Tal, M. Kiguchi, W. H. A. Thijssen, D. Djukic, C. Untiedt, R. H. M. Smit and J. M. V. Ruitenbeek, *Phys. Rev. B*, 2009, **80**, 1–8.

6 P. Makk, Z. Balogh, S. Csonka and A. Halbritter, *Nanoscale*, 2012, **4**, 4739–45.

7 S. V. Aradhya, M. Frei, A. Halbritter and L. Venkataraman, *ACS Nano*, 2013, **7**, 3706–3712.

8 T. Kim, H. Vázquez, M. S. Hybertsen and L. Venkataraman, *Nano Lett.*, 2013, **13**, 3358–3364.

9 X. Guo, J. P. Small, J. E. Klare, Y. Wang, M. S. Purewal, I. W. Tam, B. H. Hong, R. Caldwell, L. Huang, S. O'brien, J. Yan, R. Breslow, S. J. Wind, J. Hone, P. Kim and C. Nuckolls, *Science*, 2006, **311**, 356–9.

10 C. W. Marquardt, S. Grunder, A. Błaszczyk, S. Dehm, F. Hennrich, H. V. Löhneysen, M. Mayor and R. Krupke, *Nat. Nanotechnol.*, 2010, **5**, 863–7.

11 C. Thiele, H. Vieker, A. Beyer, B. S. Flavel, F. Hennrich, D. Muñoz Torres, T. R. Eaton, M. Mayor, M. M. Kappes, A. Gölzhäuser, H. V. Löhneysen and R. Krupke, *Appl. Phys. Lett.*, 2014, **104**, 103102.

12 F. Prins, A. Barreiro, J. W. Ruitenberg, J. S. Seldenthuis, N. Aliaga-Alcalde, L. M. K. Vandersypen and H. S. J. van der Zant, *Nano Lett.*, 2011, **11**, 4607–11.

13 G. Wang, Y. Kim, M. Choe, T.-W. Kim and T. Lee, *Adv. Mater.*, 2011, **23**, 755–60.

14 Y. Wen, J. Chen, Y. Guo, B. Wu, G. Yu and Y. Liu, *Adv. Mater.*, 2012, **24**, 3482–5.

15 Y. Cao, S. Dong, S. Liu, L. He, L. Gan, X. Yu, M. L. Steigerwald, X. Wu, Z. Liu and X. Guo, *Angew. Chem., Int. Ed.*, 2012, **51**, 12228–32.

16 S. Seo, M. Min, S. M. Lee and H. Lee, *Nat. Commun.*, 2013, **4**, 1920.

17 W. Fu, C. Nef, O. Knopfmacher, A. Tarasov, M. Weiss, M. Calame and C. Schönenberger, *Nano Lett.*, 2011, **11**, 3597–600.

18 W. Fu, C. Nef, A. Tarasov, M. Wipf, R. Stoop, O. Knopfmacher, M. Weiss, M. Calame and C. Schönenberger, *Nanoscale*, 2013, **5**, 12104–10.

19 X. Li, W. Cai, J. An, S. Kim, J. Nah, D. Yang, R. Piner, A. Velamakanni, I. Jung, E. Tutuc, S. K. Banerjee, L. Colombo and R. S. Ruoff, *Science*, 2009, **324**, 1312–4.

20 Y. Lee, S. Bae, H. Jang, S. Jang, S.-E. Zhu, S. H. Sim, Y. I. Song, B. H. Hong and J.-H. Ahn, *Nano Lett.*, 2010, **10**, 490–3.

21 C. Mattevi, H. Kim and M. Chhowalla, *J. Mater. Chem.*, 2011, **21**, 3324.

22 K. V. Emtsev, A. Bostwick, K. Horn, J. Jobst, G. L. Kellogg, L. Ley, J. L. McChesney, T. Ohta, S. a. Reshanov, J. Röhrl, E. Rotenberg, A. K. Schmid, D. Waldmann, H. B. Weber and T. Seyller, *Nat. Mater.*, 2009, **8**, 203–7.

23 D. Carrascal, V. García-Suárez and J. Ferrer, *Phys. Rev. B*, 2012, **85**, 195434.

24 D. Ryndyk, J. Bundesmann, M.-H. Liu and K. Richter, *Phys. Rev. B*, 2012, **86**, 195425.

25 C. G. Péterfalvi and C. J. Lambert, *Phys. Rev. B*, 2012, **86**, 085443.

26 E. Burzurí, F. Prins and H. S. J. van der Zant, *Graphene*, 2012, **01**, 26–29.

27 D. C. Bell, M. C. Lemme, L. a. Stern, J. R. Williams and C. M. Marcus, *Nanotechnology*, 2009, **20**, 455301.

28 A. Abbas, G. Liu, B. Liu, L. Zhang and H. Liu, *ACS Nano*, 2014, **8**, 1538–1546.

29 N. Kalhor, S. a. Boden and H. Mizuta, *Microelectron. Eng.*, 2014, **114**, 70–77.

30 A. Barreiro, F. Börrnert, M. H. Rümmeli, B. Büchner and L. M. K. Vandersypen, *Nano Lett.*, 2012, **12**, 1873–8.

31 F. Börrnert, A. Barreiro, D. Wolf, M. I. Katsnelson, B. Büchner, L. M. K. Vandersypen and M. H. Rümmeli, *Nano Lett.*, 2012, **12**, 4455–9.

32 B. Standley, W. Bao, H. Zhang, J. Bruck, C. N. Lau and M. Bockrath, *Nano Lett.*, 2008, **8**, 3345–9.

33 S.-F. Shi, X. Xu, D. C. Ralph and P. L. McEuen, *Nano Lett.*, 2011, **11**, 1814–8.

34 J. Moser and a. Bachtold, *Appl. Phys. Lett.*, 2009, **95**, 173506.

35 A. Barreiro, H. S. J. van der Zant and L. M. K. Vandersypen, *Nano Lett.*, 2012, **12**, 6096–100.

36 P. Collins, M. Hersam, M. Arnold, R. Martel and P. Avouris, *Phys. Rev. Lett.*, 2001, **86**, 3128–3131.

37 M. Freitag, M. Steiner, Y. Martin, V. Perebeinos, Z. Chen, J. C. Tsang and P. Avouris, *Nano Lett.*, 2009, **9**, 1883–8.

38 D.-H. Chae, B. Krauss, K. von Klitzing and J. H. Smet, *Nano Lett.*, 2010, **10**, 466–71.

39 X. Li, Y. Zhu, W. Cai, M. Borysiak, B. Han, D. Chen, R. D. Piner, L. Colombo and R. S. Ruoff, *Nano Lett.*, 2009, **9**, 4359–63.

40 J. W. Suk, A. Kitt, C. W. Magnuson, Y. Hao, S. Ahmed, J. An, A. K. Swan, B. B. Goldberg and R. S. Ruoff, *ACS Nano*, 2011, **5**, 6916–24.

41 Z. M. Wu, M. Steinacher, R. Huber, M. Calame, S. J. van der Molen and C. Scho?nenberger, *Appl. Phys. Lett.*, 2007, **91**, 053118.

42 A. Barreiro, M. Lazzeri, J. Moser, F. Mauri and A. Bachtold, *Phys. Rev. Lett.*, 2009, **103**, 2–5.

43 M.-H. Bae, Z.-Y. Ong, D. Estrada and E. Pop, *Nano Lett.*, 2010, **10**, 4787–4793.

44 R. A. Cowley, *J. Phys. (Paris)*, 1965, **26**, 659–667.

45 M. Balkanski, R. F. Wallis and E. Haro, *Phys. Rev. B*, 1983, **28**, 1928–1934.

46 J. Moser, a. Barreiro and a. Bachtold, *Appl. Phys. Lett.*, 2007, **91**, 163513.

47 A. Barreiro, R. Rurali, E. R. Hernández and A. Bachtold, *Small*, 2011, **7**, 775–80.

48 N. Tombros, A. Veligura, J. Junesch, M. H. D. Guimarães, I. J. Vera-Marun, H. T. Jonkman and B. J. van Wees, *Nat. Phys.*, 2011, **7**, 697–700.

49 P. Rickhaus, R. Maurand, M.-H. Liu, M. Weiss, K. Richter and C. Schönenberger, *Nat. Commun.*, 2013, **4**, 2342.

50 A. L. Grushina, D.-K. Ki and A. F. Morpurgo, *Appl. Phys. Lett.*, 2013, **102**, 223102.

51 I. Calizo, F. Miao, W. Bao, C. N. Lau and A. a. Balandin, *Appl. Phys. Lett.*, 2007, **91**, 071913.

52 L. Liu, S. Ryu, M. R. Tomasik, E. Stolyarova, N. Jung, M. S. Hybertsen, M. L. Steigerwald, L. E. Brus and G. W. Flynn, *Nano Lett.*, 2008, **8**, 1965–70.

53 V. E. Dorgan, A. Behnam, H. J. Conley, K. I. Bolotin and E. Pop, *Nano Lett.*, 2013, **13**, 4581–6.

54 A. a. Balandin, *Nat. Mater.*, 2011, **10**, 569–81.

55 M.-H. Bae, Z. Li, Z. Aksamija, P. N. Martin, F. Xiong, Z.-Y. Ong, I. Knezevic and E. Pop, *Nat. Commun.*, 2013, **4**, 1734.

56 J.-H. Chen, C. Jang, S. Xiao, M. Ishigami and M. S. Fuhrer, *Nat. Nanotechnol.*, 2008, **3**, 206–9.

57 S. Fratini and F. Guinea, *Phys. Rev. B*, 2008, **77**, 195415.

58 a. S. Price, S. M. Hornett, a. V. Shytov, E. Hendry and D. W. Horsell, *Phys. Rev. B*, 2012, **85**, 161411.

59 D. K. Efetov and P. Kim, *Phys. Rev. Lett.*, 2010, **105**, 256805.

60 J. G. Simmons, *J. Appl. Phys.*, 1963, **34**, 1793.

Nanoscale Accepted Manuscript